Cyclic steps and roll waves in shallow water flow over an erodible bed

N. J. Balmforth[1,2] and A. Vakil[1]†

[1] Department of Mathematics, University of British Columbia, Vancouver, BC Canada V6T 1Z2

[2] Earth and Ocean Science, University of British Columbia, Vancouver, BC Canada V6T 1Z4

The St Venant equations in conjunction with a phenomenological law for erosion are used to explore the nonlinear dynamics of cyclic steps – linearly unstable bedform patterns which emerge when uniform flow over an erodible bed becomes supercritical. The instability saturates by blocking the overlying flow and creating hydraulic jumps just downstream of the steepest part of the steps. Near onset, steadily migrating, nonlinear step patterns are constructed and shown to suffer a short-wavelength secondary instability that 'roughens' the bed and renders the staircase patterns less regular and time-dependent. An eddy viscosity is needed to regularize both the onset of the primary steps and the secondary instabilities. Further beyond the critical Froude number, the steps block the flow sufficiently to arrest erosion significantly, creating complicated patterns mixing migrating steps and stationary bedforms. The reduction in flux also stabilizes roll waves – a second, hydrodynamic instability of uniform supercritical flow. It is further shown that roll waves are purely convective instabilities, whereas cyclic steps can be absolute. Thus, in the finite geometries of the laboratory or field, it may be difficult to excite roll waves. On the other hand, the complicated spatiotemporal patterns associated with the cyclic-step instability should develop naturally. The complicated patterns resulting from the secondary instability do not appear to have been observed experimentally, calling into question the validity of the model.

Key words: absolute/convective instability, bifurcation, shallow water flows

---

1. Introduction

Cyclic steps are upstream-migrating erosional features that have been reported on the bed of natural streams and turbidity currents (e.g. Kostic *et al.* 2010) and successfully reproduced in laboratory experiments (e.g. Koyama & Ikeda 1998; Taki & Parker 2005). Much like many other bedform patterns in geomorphology, these steps have been rationalized from a theoretical perspective in terms of a linear instability of spatially uniform flow, occurring due to the interaction between the erodible bed and the overlying fluid dynamics (Parker & Izumi 2000). As elucidated by Parker (2008), cyclic steps are closely related to a more classical erosional instability, the antidune; the cyclic steps are distinguished by their long-lived and long-wave character, whereas antidunes are typically short-wave.

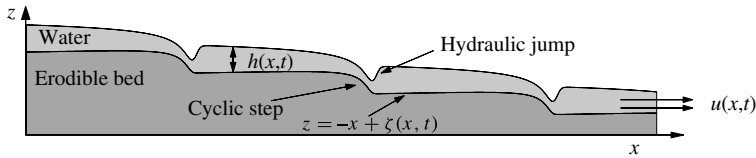† Email address for correspondence: ali.vakil@gmail.com

FIGURE 1. Sketch of the geometry of the shallow-water model, showing the three key dynamical variables (h, u and ζ) and a sample sequence of theoretical cyclic-step profiles, together with their associated hydraulic jumps.

By combining the St Venant equations of hydraulic engineering for the fluid with a phenomenological sediment transport equation to model the bed, Parker & Izumi (2000) established that a linear instability corresponding to cyclic steps appears when uniform flow becomes supercritical (the Froude number, Fr, exceeds unity). The instability operates on the relatively slow time scale of erosion and has upstream phase propagation, highlighting its erosional and upstream-migrating character. Parker & Izumi also constructed finite-amplitude, steady, periodic step solutions. A key detail of their solutions is that each step modifies the overlying water flow and creates hydraulic jumps just downstream of the steepest part of the bedforms (as sketched in figure 1). Upstream of these shocks, flow remains supercritical and erosion (which increases with water speed) is greatest; immediately downstream of the shocks, the flow is subcritical, and erosion is at a minimum. It is this pattern of erosion which drives the upstream migration of the cyclic steps (see also Winterwerp *et al.* 1992). Parker & Izumi further selected the wavelength of the step sequence by demanding that flow speeds just downstream of the hydraulic jumps lie at the threshold below which erosion switches off, arguing that this places a natural nonlinear limit on a developing linear step instability.

Nevertheless, no studies have been made to back up the assumption that the nonlinear saturation of the step instability produces periodic sequences of steadily migrating steps of this kind, and a systematic exploration of the detailed nonlinear dynamics has not previously been given. The goal of the current article is to provide such an exploration using the relatively simple theoretical framework of Parker & Izumi. In fact, we find that this model does not predict the emergence of steadily migrating, periodic step sequences, but suggests that the dynamics is much richer. The only other theoretical works on cyclic steps, of which we are aware, proceed in a different direction: Sun & Parker (2005) generalized Parker & Izumi's work to include the effects of deposition, and Fagherazzi & Sun (2003) presented a small number of numerical computations using that theoretical model.

In addition to cyclic steps, supercritical shallow-water flow over an erodible bed is also known to be prone to a second type of linear instability, roll waves. These instabilities have hydrodynamic origin, operating on the relatively fast time scale of the fluid flow, and in the nonlinear regime take the form of downstream-propagating bores (Cornish 1910). Balmforth & Mandre (2004) presented a study of the nonlinear dynamics of roll waves using the St Venant model, and also explored how these waves interacted with bed topography. In particular, Balmforth & Mandre found that roll-wave stability was significantly affected by the stationary hydraulic jumps that often arise in flow over an uneven bed. This raises the question of how cyclic steps, themselves a form of linear instability, might interact with roll waves given that they also generate hydraulic jumps. The current article therefore offers a brief exploration of the interaction between roll waves and cyclic steps. Colombini & Stocchino (2005)

presented a related study of the competition between roll waves and other erosional instabilities within linear theory, without the simplifying shallow-water approximation and using a different model for sediment transport.

The article is organized as follows: in §2, we formulate the problem mathematically. Section 3 is then devoted to a discussion of linear stability, from both the convective and absolute viewpoints. In §4, we present an asymptotic analysis valid near the onset of linear instability. In §5, we advance further into the nonlinear regime, solving numerically the governing equations of the model, and we conclude in §6. The sediment transport model used in the main text incorporates only the erosion of the bed by the overlying flow; a more physical extension of the model which includes the effects of deposition is discussed in appendix A. Technical details of the analytical construction of some weakly nonlinear solutions appear in appendix B.

2. Formulation

2.1. *The model equations*

Our model for shallow-water flow over an inclined erodible bed couples the St Venant model of hydraulic engineering to a sediment transport model advocated by Parker & Izumi (2000). As illustrated in figure 1, the key variables of the model are the water depth, $h(x, t)$, and speed, $u(x, t)$, and the height of the bed, $-x \tan \theta + \zeta(x, t)$, where $\tan \theta$ denotes the average inclination of the bed's surface to the horizontal. With a suitable scaling, these variables can be rendered dimensionless, and the governing equations of the model written in the form

$$h_t + (hu)_x = 0, \tag{2.1}$$

$$Fr^2(u_t + uu_x) = 1 - \frac{|u|u}{h} - h_x - \zeta_x + \frac{1}{h}(\nu h u_x)_x \tag{2.2}$$

and

$$\zeta_t = -\varepsilon \mathscr{E}(u), \tag{2.3}$$

representing conservation of fluid mass and momentum, and the empirical erosion law (an Exner equation), with the (x, t)-subscripts denoting partial derivatives. The dimensionless parameters are the Froude number, Fr, a dimensionless eddy viscosity, ν (assumed constant here), and an erosion rate, ε; the dependence of erosion on flow speed is parameterized by

$$\mathscr{E}(u) = \begin{cases} (u^2 - u_*^2)^m, & u^2 \geqslant u_*^2, \\ 0, & u^2 < u_*^2, \end{cases} \tag{2.4}$$

where u_* is a threshold erosion speed and the exponent, m, is set equal to 2 here.

Note that the shallow-water equations do not incorporate any source of mass or sink of momentum occurring when sediment is eroded off the bed. Also, (2.3) ignores deposition; sediment suspended in the water column is assumed (somewhat unphysically) to remain there and never return to the bed. Following Fagherazzi & Sun (2003) and Sun & Parker (2005), one can supplement the system (2.1)–(2.4) with a further equation for the suspended load and thereby account for deposition; appendix A provides additional commentary of this extension of the model. However, for the most part, we follow Parker & Izumi (2000) and consider pure erosion, neglecting any effects of the eroded material on the flow dynamics other than through the change in bed slope.

To arrive at (2.1)–(2.4), we scale the water depth and bed elevation by a characteristic mean depth, H, horizontal lengths by $H \cot\theta$ and the flow speed by $U = \sqrt{gH \sin\theta / c_f}$, where g is the gravitational acceleration and c_f is the coefficient of the Chézy drag (the second term on the right of (2.2)). In terms of these characteristic scales, the Froude number is $Fr = \sqrt{U^2/gH \cos\theta} \equiv \sqrt{\tan\theta / c_f}$ and the elevation of the bed is $-x + \zeta$; the dimensionless eddy viscosity is $\nu = \nu_t \tan^2\theta / \sqrt{gH^3 c_f \sin\theta}$, where ν_t is the dimensional eddy viscosity. Moreover, the system (2.1)–(2.3) admits the equilibrium solution

$$h = u = 1, \quad \zeta = -\varepsilon t \mathscr{E}(1), \tag{2.5}$$

denoting a uniform flow with a steadily eroding bed.

An important difference between our formulation and that of Parker and coworkers (Parker & Izumi 2000; Sun & Parker 2005) is the inclusion of the time derivatives in the fluid equations and the eddy diffusion term in (2.2). Although cyclic steps develop on a much slower erosion time scale, the hydrodynamic time derivatives are needed to consider roll waves (see also Colombini & Stocchino 2005). The viscous term allows us to damp very short wavelengths and smooth out any hydraulic jumps *via* a physically based regularization, thereby easing numerical solution of the initial-value problem and allowing us to explore the dynamics in the vicinity of the onset of cyclic-step instability. We emphasize that our main intention is not to explore the effect of different turbulence models on cyclic-step formation, and we chiefly add the eddy viscosity term in (2.2) as a convenient regularization of the equation. The prescription is nothing more than a crude parameterization of turbulence, and follows similar idealizations by Needham & Merkin (1984) and Kranenburg (1992). Nevertheless, dimensional analysis or depth averages of the fluid momentum equations suggest that an arguably more natural (if still crude) choice for the dimensional eddy viscosity, ν_t, renders that quantity non-constant and proportional to the water flux; in dimensionless form, one sets $\nu = \nu_T h|u|$ in (2.2), where $\nu_T = \Lambda Fr^2 \tan\theta \equiv \Lambda Fr^4/c_f$ and Λ is a constant of order unity. For the most part, and in the interest of simplicity, our discussion treats ν as a constant parameter that is independent of Froude number. However, we did perform a complementary set of computations in which we incorporated the alternative eddy viscosity model with $\nu = \nu_T h|u|$. We found no qualitative difference between the two models in the nonlinear evolution of the bedforms, at least for the parameter choices we selected (with Λ chosen as ν/Fr^4, to match the eddy viscosities of the base flows), with the main quantitative difference being that the secondary instability studied in §5.2 became slightly more pronounced and shorter scale; for higher Froude numbers, the primary cyclic steps also became noticeably steeper. As discussed further in §3.2, the modified eddy viscosity is straightforwardly incorporated into linear stability theory with the shallow-water model (see §3.2). Moreover, the modification does not alter the weakly viscous, multiple-scale analysis of §4. In other words, provided one incorporates an eddy viscosity term of some kind, the model is regularized in a way that is independent of the precise form of that term.

2.2. *Numerical method*

We mostly solve the system (2.1)–(2.3) on a periodic domain of length L and begin from initial conditions consisting of small, random perturbations about the steadily eroding, uniform flow. More specifically, unless otherwise stated, $h(x, 0) = 1$, $u(x, 0) = 1 + \check{u}(x)$ and $\zeta(x, 0) = \check{\zeta}(x)$, where $\check{u}$ and $\check{\zeta}$ are low-amplitude (order 10^{-3}), wavy perturbations given by a random superposition of the first 20 Fourier modes.

For the numerical solution of the initial-value problem, we use centred finite differences on a uniform grid to deal with spatial derivatives, and then solve the resulting system of ordinary differential equations with a standard, stiff integrator with variable time step (DASSL; Petzold 1983). Typically, we use of the order of 10^3 points, verifying that there are no significant changes in the solutions if the spatial resolution is changed. We also verified that the solutions are insensitive to improvements in the error tolerance of the time integrator (which use the defaults of 10^{-3} as a relative tolerance and 10^{-6} as an absolute one), and do not change when the centred differencing of the advection terms is replaced by a first-order upwind scheme.

To solve the differential eigenvalue problem for steady cyclic steps (§ 5.1), we use MATLAB's BVP4c solver, which uses an adaptive step strategy to reduce errors below a predefined tolerance (we used 10^{-5} as a relative tolerance and 10^{-10} as an absolute one). The linear stability of those solutions (see § 5.2) was determined by resampling the solution on a uniform grid of $\sim 10^3$ points and using the centred difference scheme once again to convert the linear system into a matrix eigenvalue problem.

In practice, we fix the erosion threshold, $u_* = 0.5$, and exponent, $m = 2$, and use the Froude number, Fr, and domain length, L, as our main control parameters. The eddy viscosity is mostly kept constant, though increases slightly with Froude number in order to ensure that solutions remain well resolved (see also the discussion at the end of § 2.1). We fix $\varepsilon = 0.1$ for many of the calculations; this value for erosion is artificially large in comparison to most physical situations. However, we make this selection to avoid overly long integration times when studying the erosion dynamics (which is characterized by time scales of order ε^{-1}), and have verified, by performing complementary calculations with smaller values for ε, that the predictions are not dependent on that choice. Similarly, we have run computations with different values for the erosion threshold to demonstrate that the qualitative character of the solutions is also not dependent on that parameter.

Near the conclusion of our study, we also consider non-periodic domains; we delay describing the salient details of those calculations until § 5.4.

3. Linear stability

3.1. *The dispersion relation*

To test the linear stability of the uniformly eroding equilibrium solution, we look for normal modes of the form

$$h = 1 + \hat{h}e^{ikx + \lambda t}, \quad u = 1 + \hat{u}e^{ikx + \lambda t}, \quad \zeta = -\varepsilon \mathscr{E}(1)t + \hat{\zeta}e^{ikx + \lambda t}, \tag{3.1}$$

where k is the wavenumber and λ the growth rate. A little algebra generates the dispersion relation

$$
\begin{aligned}
D(k, \lambda) = Fr^2\lambda^3 + \lambda^2(2 + \nu k^2 + 2ikFr^2) + \lambda[k^2(1 - Fr^2) + ik(3 + \nu k^2 - \alpha)] \\
+ \alpha k^2 = 0,
\end{aligned}
\tag{3.2}
$$

where $\alpha = \varepsilon \mathscr{E}'(1)$.

The limit $\varepsilon \ll 1$ and $\lambda = O(\varepsilon)$, with all other parameters of order one, corresponds to the 'quasisteady' limit of the problem often explored in geomorphological studies (e.g. Parker & Izumi 2000), in which case

$$D(k, \lambda) \to \lambda[k^2(1 - Fr^2) + ik(3 + \nu k^2)] + \alpha k^2 \approx 0 \tag{3.3}$$

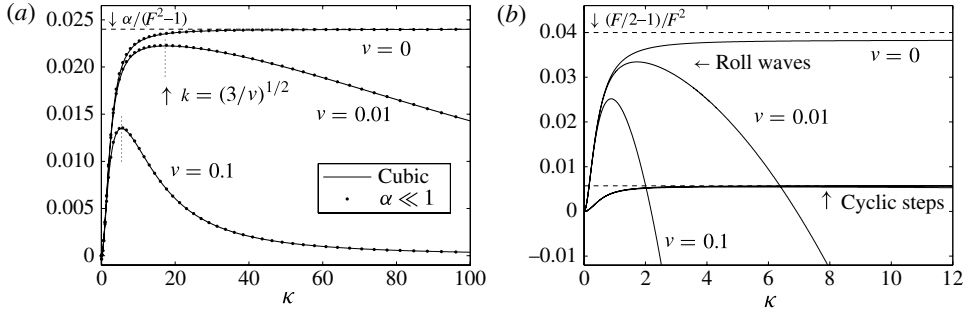FIGURE 2. Growth rates for (*a*) $Fr = 1.5$ and (*b*) $Fr = 2.5$, $\varepsilon = 0.01$ and the three values of ν indicated. In (*a*), only cyclic-step modes are unstable, the dots show the growth rates predicted by the $\alpha \ll 1$ approximation of the dispersion relation in (3.4) and the vertical dotted line indicates the most unstable wavenumber ($k \approx \sqrt{3/\nu}$). In (*b*), both cyclic-step modes and roll waves are unstable; the former are insensitive to the choice of ν for the wavenumbers shown. In (*a*) and (*b*), the large-wavenumber limits of the inviscid growth rates are indicated by horizontal dashed lines ($\lambda \to \alpha/(Fr^2 - 1)$ and $\lambda \to (Fr - 2)/(2Fr^2)$ for cyclic steps and roll waves, respectively).

or

$$\lambda \approx \frac{\alpha[k^2(Fr^2 - 1) + ik(3 + \nu k^2)]}{k^2(Fr^2 - 1)^2 + (3 + \nu k^2)^2}. \tag{3.4}$$

3.2. *Stability boundaries and growth rates*

Neutral stability conditions follow by introducing $\lambda = -ikc$, where c is the wave speed. Separating real and imaginary parts of (3.2) then furnishes the possible values for c, together with the critical Froude number, $Fr = Fr_c$:

$$(2 + \nu k^2)c^2 - c(3 + \nu k^2 - \alpha) - \alpha = 0, \quad (1 - c)^2 Fr_c^2 = 1. \tag{3.5}$$

For $\alpha \ll 1$ and $\nu \ll 1$ (the physical regime of interest), the two roots provide the stability conditions, $(c, Fr_c) \sim (3/2, 2)$ or $(c, Fr_c) \sim (-\alpha/3, 1)$. The first is the classical roll-wave instability threshold (Jeffreys 1925), whilst the second corresponds to Parker & Izumi's (2000) cyclic steps. In both cases, instability appears when the Froude number is raised above the threshold value. Roll waves travel downstream faster than the flow, whereas the cyclic steps migrate slowly upstream. No other types of instability are apparent from the dispersion relation or neutral stability curves; the exploration of more classical erosional instabilities of the dune or antidune type requires a different model for sediment transport and the relaxation of the shallow-water approximation for the fluid (cf. Colombini & Stocchino 2005).

Growth rates for the two instabilities are illustrated in figure 2. Figure 2(*a*) shows cyclic-step growth rates for $Fr = 1.5$, roll waves being stable at that Froude number. figure 2(*b*) displays the growth rates of both instabilities at $Fr = 2.5$. For both cyclic steps and roll waves, the viscous term in the momentum equation stabilizes modes with large wavenumber, leading to a maximum in the growth rates as a function of k. The roll-wave growth rates acquire a cutoff that limits the range of unstable wavenumbers. By contrast, for cyclic steps all wavelengths become unstable when $Fr > 1$.
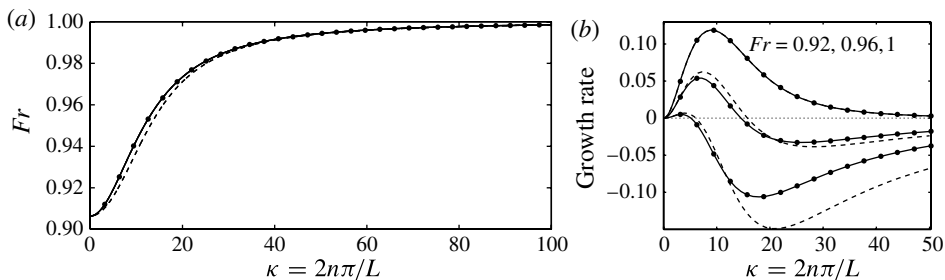
FIGURE 3. (*a*) Stability boundary, $Fr = Fr_c$, and (*b*) growth rates against k for $\nu = 0.02$ and $\varepsilon = 0.1$. In (*b*), the growth rates are plotted for the three values of Fr indicated. The dots indicate the wavenumbers for a periodic domain of length 2 ($k = n\pi$, $n = 1, 2, \ldots$). The dashed lines in (*a*) and (*b*) indicate the corresponding results using the alternative model for eddy viscosity, $\nu = 0.02 Fr^4 h|u|$ (equivalent to replacing ν by $0.02 Fr^4$ in (3.2)–(3.5)).

More disturbingly, if $\nu = 0$, one can compute the maximum growth rate from (3.4), $\mathrm{Re}(\lambda) = \alpha/(Fr^2 - 1)$, which occurs for short waves with $k \gg 3/(Fr^2 - 1)$ and diverges at onset. This problematic behaviour is regularized if $\nu \neq 0$: the maximum growth rate, $\mathrm{Re}(\lambda) = \alpha(Fr^2 - 1)/[12\nu + (Fr^2 - 1)^2]$, arises for a wavenumber of $k = \sqrt{3/\nu}$ and remains finite at onset. Thus, in order to explore pattern formation in this regime and regularize the dynamics, it is important to include the viscous term.

As displayed in figure 3, the cyclic-step instability also extends to Froude numbers slightly below unity. Indeed, for $k \to 0$ and $\alpha \ll 1$, the critical conditions in (3.5) indicate that $Fr_c \approx 1 - \alpha/3 \equiv 1 - \varepsilon$ for $m = 2$ and $u_* = 0.5$ (implying $\alpha = \varepsilon \mathscr{E}'(1) = 3\varepsilon$). Figure 3 also illustrates how, for $Fr_c < 1$, the range of unstable wavenumbers is finite.

Note that if one adopts the alternative eddy viscosity model with $\nu = \nu_T h|u|$, the linear stability theory is unchanged but for the replacement, $\nu = \nu_T = \Lambda Fr^4/c_f$, in (3.2)–(3.5). For given Λ and c_f, the viscosity parameter is therefore dependent on the Froude number, obscuring the neutral stability conditions in (3.5). However, for the range of Froude numbers covered in figure 3, the repercussions on the stability properties are not significant, as illustrated by the additional data for $\nu = 0.02 Fr^4$ that are also included in the figure.

3.3. *Convective and absolute instability*

For roll waves without erosion, one expects instability to be convective: when flow is supercritical ($Fr > 1$), the Riemann invariants of the characteristic problem for the St Venant equations are propagated purely downstream, indicating that any disturbance must be swept along with the flow. On the other hand, in the linearized erosive problem, the slow 'sediment mode' propagates upstream even under supercritical conditions, leading one to suspect that it is an absolute instability. To expose these features more clearly, we look for saddle points of the dispersion function $D(k, \lambda)$ (cf. Briggs 1964).

For $\nu \ll 1$, it turns out to be possible to rule out the existence of saddle points with real frequency: in this limit,

$$\frac{\partial D}{\partial k} = 2\mathrm{i}\lambda^2 Fr^2 + \lambda[2k(1 - Fr^2) + \mathrm{i}(3 - \alpha)] + 2\alpha k. \tag{3.6}$$

Setting $\partial D/\partial k = 0$ and $\lambda = i\omega$ then indicates that

$$k = \frac{\omega}{2}\left[\frac{2i\omega Fr^2 + 3 - \alpha}{\alpha + i\omega(1 - Fr^2)}\right]. \tag{3.7}$$

Introducing this wavenumber back into the $\nu = 0$ dispersion relation and separating the imaginary part leads to the impossible condition $2 + Fr^2 = 0$. Thus, there cannot be a transition to absolute instability at any Froude number, indicating that roll waves must be convective (except possibly at very short wavelengths, for which νk^2 is of order one).

The picture is not so straightforward for cyclic steps, however, as we illustrate by taking the limit, $\alpha \ll 1$ and $\lambda \sim \alpha$, with $\nu \neq 0$. In this limit, the dispersion relation reduces to (3.3) and

$$\frac{\partial D}{\partial k} \approx \frac{D}{k} + k[\alpha + \lambda(1 - Fr^2) + 2i\nu\lambda k]. \tag{3.8}$$

Setting $D = \partial D/\partial k = 0$ implies that

$$12\nu\lambda^2 + [\alpha + \lambda(1 - Fr^2)]^2 = 0 \quad \text{and} \quad k = \frac{i}{2\nu\lambda}[\alpha + \lambda(1 - Fr^2)] = \pm\sqrt{\frac{3}{\nu}}, \tag{3.9}$$

so that

$$\text{Re}(\lambda) = \frac{\alpha(Fr^2 - 1)}{12\nu + (1 - Fr^2)^2}. \tag{3.10}$$

Thus, there is a saddle point of the dispersion relation with positive growth rate for $Fr > 1$. Moreover, that solution corresponds to the most unstable mode from (3.4) described earlier. Note that this point behaves irregularly in the limit $\nu \to 0$, which is why it does not appear earlier in the $\nu = 0$ analysis. We conclude that cyclic steps are potentially unstable in an absolute sense if $Fr > 1$ (the existence of the saddle point is necessary, but not sufficient, for absolute instability; see Briggs 1964). We confirm this prediction later using numerical computations.

4. Multiple-scale analysis

Yu & Kevorkian (1992) and Balmforth & Mandre (2004) presented multiple-scale analyses describing the onset of roll-wave instability for the St Venant equations with a fixed bed. In this section, we generalize those asymptotic expansions to include erosion.

4.1. *Asymptotic expansion*

To describe the dynamics close to the onset of instability, we set $\partial_t \to \partial_t + \delta\partial_T$, where t is the relatively fast (order-one) time on which a neutrally stable disturbance propagates, T is the slow time on which that wave-like disturbance will amplify and δ is the small parameter used to organize the asymptotic expansion. We displace parameter settings from the marginal values by putting $Fr^2 = Fr_c^2 + \delta f$ and fix $\nu = \delta\nu_1$ to ensure a weakly viscous solution. We then introduce the asymptotic sequences

$$h = 1 + \delta h_1(x, t, T) + \delta^2 h_2(x, t, T) + \cdots, \quad u = 1 + \delta u_1(x, t, T) + \delta^2 u_2(x, t, T) + \cdots, \tag{4.1}$$

$$\zeta = -\varepsilon\mathscr{E}(1)t + \delta\zeta_1(x, t, T) + \delta^2\zeta_2(x, t, T) + \cdots \tag{4.2}$$

into the governing equations and solve the resulting hierarchy order by order in δ.

At leading order,

$$h_{1t} + h_{1x} + u_{1x} = 0, \tag{4.3}$$

$$Fr_c{}^2(u_{1t} + u_{1x}) + h_{1x} + \zeta_{1x} - h_1 + 2u_1 = 0, \tag{4.4}$$

$$\zeta_{1t} + \alpha u_1 = 0. \tag{4.5}$$

These equations have solutions with the form of neutrally stable waves: introducing $h_1 = h_1(x - ct, T)$, $u_1 = u_1(x - ct, T)$ and $\zeta_1 = \zeta_1(x - ct, T)$, we find

$$u_1 = -(1 - c)h_1, \quad \zeta_{1x} = \frac{\alpha}{c}(1 - c)h_1 \tag{4.6}$$

and then

$$[1 - Fr_c{}^2 (c - 1)^2]h_{1x} + \left[2c - 3 - \frac{\alpha}{c}(1 - c)\right] h_1 = 0, \tag{4.7}$$

which is satisfied automatically by virtue of the $\nu = 0$ critical conditions in (3.5).

At the following order, we obtain

$$h_{2t} + h_{2x} + u_{2x} = -h_{1T} - (h_1 u_1)_x, \tag{4.8}$$

$$Fr_c{}^2(u_{2t} + u_{2x}) + h_{2x} + \zeta_{2x} - h_2 + 2u_2 = \nu_1 u_{1xx} - f(1 - c)u_{1x} - Fr_c{}^2(u_{1T} + u_1 u_{1x})$$
$$- u_1^2 + 2h_1 u_1 - h_1^2, \tag{4.9}$$

$$\zeta_{2t} + \alpha u_2 = -\zeta_{1T} - \beta u_1^2, \tag{4.10}$$

where $\beta = \varepsilon \mathcal{E}''(1)/2$. Using the critical conditions and again searching for wave solutions with dependence $x - ct$, we may then eliminate the second-order variables, h_2, u_2 and ζ_2, to arrive at the equation

$$\left[\frac{1 + 2(1 - c)^2}{c} - 2\partial_x\right] h_{1T} = (1 - c)^3 fh_{1xx} - \nu_1 (1 - c)^2 h_{1xxx} - \frac{3}{2}(1 - c)(h_1^2)_{xx}$$

$$- (1 - c)^2 \left[3 - c + \frac{\beta}{c}(1 - c)\right] (h_1^2)_x. \tag{4.11}$$

This equation generalizes those derived by Yu & Kevorkian (1992) and Balmforth & Mandre (2004) for roll waves. Indeed, for $F_c \to 2$ and $c \to 3/2$, we recover their equations. However, the model also describes weakly unstable cyclic-step modes and includes an additional nonlinear term. Balmforth & Mandre presented numerical solutions of the erosionless model that illustrate how linearly unstable disturbances steepen into nonlinear roll-wave trains. If the wave spacings are relatively small, these wave trains subsequently coarsen as the component waves collide with one another and merge. On the other hand, when the spacings are too wide, new roll waves grow within the gaps to reduce wavelengths. In between these limits, wave trains with intermediate spacings are stable. Thus, roll-wave patterns develop with a range of preferred wave spacings.

4.2. *Nonlinear wave solutions*

We place (4.11) into a canonical form by defining the new variables

$$\left.\begin{array}{c} x = \dfrac{c(\xi - \tau)}{1 + 2(1 - c)^2}, \quad T = -\dfrac{2c\tau}{(1 - c)^3 f[1 + 2(1 - c)^2]}, \\[2mm] h_1 = \dfrac{1}{3}(1 - c)^2 f\varphi(\xi, \tau), \end{array}\right\} \tag{4.12}$$

giving

$$(1 - 2\partial_\xi)(\varphi_\tau + \varphi\varphi_\xi) + \varphi_\xi + \mu\varphi_{\xi\xi\xi} + \gamma\varphi\varphi_\xi = 0, \qquad (4.13)$$

where

$$\left.\begin{aligned}
\mu &= -\frac{2\nu_1[1 + 2(1 - c)^2]}{c(1 - c)f}, \\
\gamma &= -1 - \left[3 - c + \frac{\beta}{c}(1 - c)\right]\frac{4c(1 - c)}{3[1 + 2(1 - c)^2]}.
\end{aligned}\right\} \qquad (4.14)$$

For roll waves with $c = 3/2$ and $\beta \to 0$, the final nonlinear term disappears because $\gamma \to 0$. For cyclic steps, $\gamma \to -1$.

In periodic domains of length $2\pi/k$, the model (4.13) predicts instability for $\mu k^2 < 1$, with the longest wave in the domain becoming unstable first as one decreases the viscous parameter μ. A straightforward weakly nonlinear analysis (given in appendix B) predicts that nonlinear waves bifurcate supercritically at this threshold. It is also possible to look for solutions to (4.13) representing non-diffusive ($\mu = 0$), steady waves with $\varphi = \varphi(\xi - C\tau)$ and speed C. As discussed in Balmforth & Mandre, these solutions contain shocks that develop when instabilities amplify and steepen. The steady-wave profiles are given by

$$\varphi = A\mathrm{e}^{(1+\gamma)(\xi - C\tau)/4} + \frac{C(1 - \gamma) - 2}{1 + \gamma}, \quad 0 < \xi - C\tau < L, \qquad (4.15)$$

with

$$C = \frac{2L(1 + \gamma) - 16\tanh[(1 + \gamma)L/8]}{L(1 - \gamma^2) + 32\tanh[(1 + \gamma)L/8]}, \quad A = \frac{4(1 + \gamma C)}{1 + \gamma}[1 + \mathrm{e}^{(1+\gamma)L/4}]^{-1}, \quad (4.16)$$

where L is the wavelength and the shocks are located at $\xi - C\tau = 0$ and L. For $\gamma \to -1$, these formulae reduce to $C = 0$ and

$$\varphi = \tfrac{1}{2}(\xi - \tfrac{1}{2}L). \qquad (4.17)$$

A numerical solution of a sample initial-value problem using (4.13) with $\gamma = -1$ is shown in figure 4. This solution is computed by using the fast Fourier transform to compute derivatives on a uniform spatial grid with 2048 points, and then integrating the resulting ordinary differential equations for the solution at each grid point using DASSL (Petzold 1983). The computation begins with a low-amplitude initial condition taking the form of the most unstable linear mode (in this case with five periods in the domain), plus a small correction to generate other wavenumbers. After a transient, the instability saturates into a nonlinear wavetrain with five, smoothed shocks. The perturbations with different periodicities continue to grow, however, disrupting that wavetrain and prompting the individual waves to collide and merge. This coarsening of the pattern continues until only a single shock remains.

Calculations like those outlined by Balmforth & Mandre further indicate that the dynamics of the nonlinear steady states for (4.13) with $\gamma = -1$ is rather different from their roll-wave relations: the periodic states with a single shock do not appear to lose stability as the domain length increases. Moreover, periodic solutions with multiple shocks never appear to become stable, always suffering wave mergers that generate the gravest wave train. In other words, the dynamics with $\gamma = -1$ takes the form of uninterrupted coarsening, as in some other model problems like the Cahn–Hilliard and real Ginzburg–Landau equations (e.g. Balmforth (1995)). However, we have not
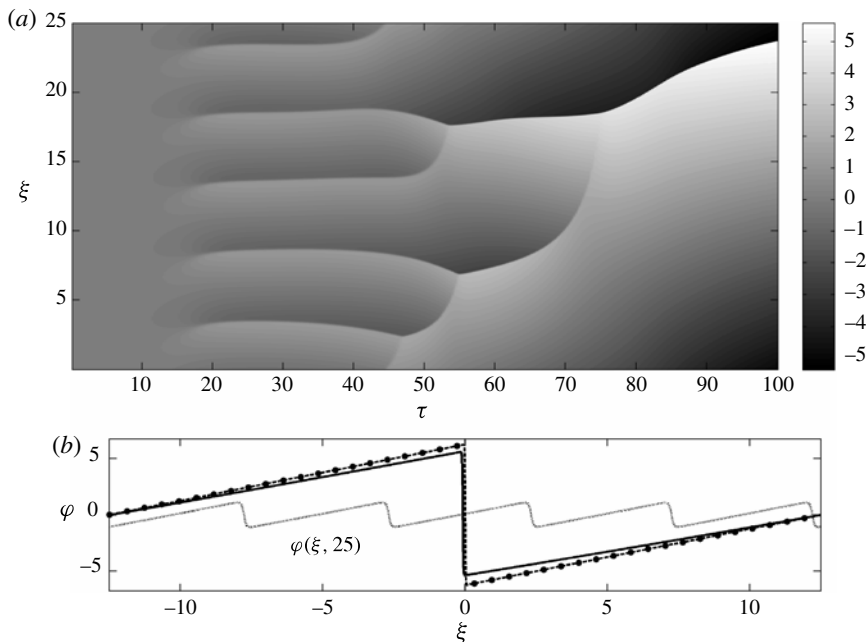
FIGURE 4. An initial-value problem using (4.13), with $\mu = 0.1$, $\gamma = -1$, $L = 25$ and $\varphi(\xi, 0) = 10^{-3} \sin(10\pi\xi/L) + 10^{-4} \sin(12\pi\xi/L)$ (the most unstable mode, plus a smaller higher mode). Panel (*a*) shows $\varphi(\xi, \tau)$ as a density on the (ξ, τ)-plane. Panel (*b*) compares the final solution (with the shock translated to $\xi = 0$; solid line) with the steady state to which the solution eventually converges over times past 100 (dashed line). The dots show the inviscid equilibrium (4.17) and the dotted line shows the intermediate, period-five solution at $t = 25$.

found any mathematical arguments to confirm this observation from a more rigourous viewpoint. In any event, the reduced model (4.13) appears less useful for cyclic steps than roll waves because it fails to capture key secondary instabilities that the nonlinear states suffer beyond onset. Instead, we provide a numerical exploration of the full system in (2.1)–(2.4).

5. Nonlinear cyclic-step dynamics
5.1. *Cyclic-step patterns near onset*
We explore the dynamics near onset by fixing the Froude number near its critical value and initiating initial-value computations by exciting at low amplitude (order 10^{-3}) one of the unstable linear modes. To gauge the strength of flow perturbations, we use the amplitude measure

$$A = \sqrt{\langle (h - 1)^2 \rangle},\tag{5.1}$$

where the angular bracket denotes spatial average,

$$\langle \cdots \rangle = \int_0^L (\cdots) \frac{dx}{L}.\tag{5.2}$$

Figure 5 shows sample results for $Fr = 0.96$ in a domain of length 2. At these parameter settings, the three most unstable modes correspond to the lowest three
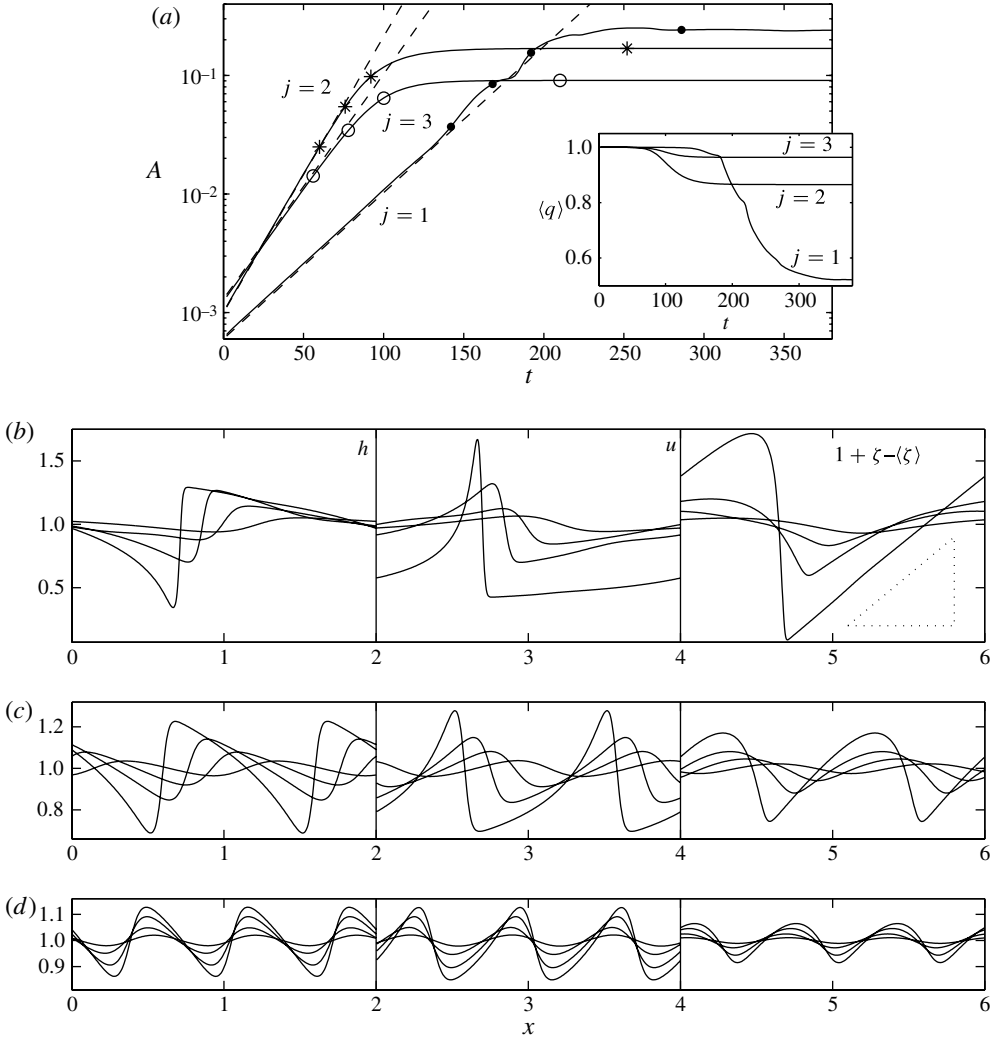
FIGURE 5. Three initial-value problems for $Fr = 0.96$, $L = 2$, $\nu = 0.02$ and $\varepsilon = 0.1$. The computations are initialized with $h = u = 1$ and $\zeta = 10^{-3}\sin(j\pi x)$, with $j = 1$, 2 and 3. Panel (*a*) shows time series of the amplitude, $A = \sqrt{\langle (h - 1)^2 \rangle}$ (solid), together with the expected linear growth for each mode (dashed). The inset shows the mean flux, $\langle q \rangle \equiv \langle hu \rangle$. The dots ($j = 1$), stars ($j = 2$) and circles ($j = 3$) mark the times of the three snapshots shown in (*b–d*), respectively; for each case, h is plotted on the left, u in the centre and $1 + \zeta - \langle \zeta \rangle$ on the right. The dotted triangle in (*b*) indicates unit slope.

wavenumbers, πj, $j = 1$, 2 and 3 (see figure 3), and, in the three computations of figure 5, these modes are (separately) kicked into action. For each case, the amplitude saturates at a steady level once nonlinear effects terminate the initial exponential growth. For the two modes with higher wavenumbers ($j = 2$ and 3), saturation occurs at an appreciable, but not excessive, level, with perturbations in depth and flow speed less than a quarter of the mean values. The gravest mode ($j = 1$), on the other hand, even though it is very close to onset and weakly unstable, grows to a relatively strong amplitude; the depth and flow speed perturbations are over one-half of the mean, and
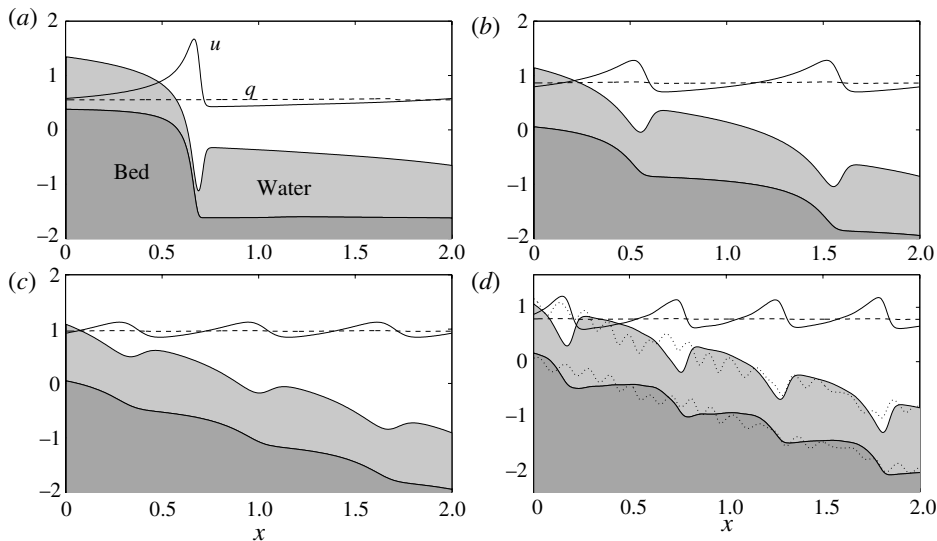
FIGURE 6. Plots of the bed (dark-shaded region, bounded above by $\zeta - \langle \zeta \rangle - x$) and water (light-shaded region, bounded above by $h + \zeta - \langle \zeta \rangle - x$), for the final states of figure 5. ((a)–(c) correspond to $j = 1$, 2 and 3, respectively.) The solid and dashed lines also show u and $q = hu$, respectively. Panel (d) shows a similar picture for part of the solution at $t = 240$ from figure 12(c); the dotted lines show the inclined bed and water surfaces for the solution at $t = 480$.

are sufficient to arrest erosion over part of the domain. However, the arrest of erosion is not critical to the nonlinear saturation process, as is clear from the computations with $j = 2$ and 3. Moreover, if the solutions are recomputed with a smaller value for u_*, even the gravest mode saturates without breaching the erosion threshold.

A different perspective on the solutions is shown in figure 6. This figure plots the surfaces of the final inclined bed, $\zeta - \langle \zeta \rangle - x$, and water, $h + \zeta - \langle \zeta \rangle - x$, along with the water speed, u, and flux, $q = hu$. At least for the first two modes, these plots emphasize how (viscously smoothed) hydraulic jumps accompany the cyclic steps. Moreover, for the gravest solution, the rearrangement of the bed almost completely levels out the topography away from the sharp step.

The saturated states in figure 5 do not persist indefinitely, as it turns out; their longer time evolution will be described shortly. However, the emergence and longevity of these states indicate that they must be close to steady equilibria. This can be confirmed by using the final profiles in figure 5 as trial solutions for computations that explicitly construct the steady travelling waves. These solutions, with $h = \mathcal{H}(\chi)$, $u = \mathcal{U}(\chi)$, $\zeta = \mathcal{Z}(\chi) - \varepsilon t \langle \mathcal{E}(\mathcal{U}) \rangle$ and $\chi = x - ct$, have constant wave speed, c, and flux in the moving frame of the wave, $\check{q} = (u - c)h$. The wave profile satisfies the nonlinear eigenvalue problem

$$\mathcal{U} = c + \frac{\check{q}}{\mathcal{H}}, \quad \frac{\mathrm{d}\mathcal{Z}}{\mathrm{d}\chi} = \frac{\varepsilon}{c}[\mathcal{E}(\mathcal{U}) - \langle \mathcal{E}(\mathcal{U}) \rangle] \tag{5.3}$$

and

$$Fr^2 \check{q} \frac{\mathrm{d}\mathcal{U}}{\mathrm{d}\chi} = \mathcal{H} - \mathcal{U}^2 - \mathcal{H}\frac{\mathrm{d}\mathcal{H}}{\mathrm{d}\chi} - \mathcal{H}\frac{\mathrm{d}\mathcal{Z}}{\mathrm{d}\chi} + \frac{\mathrm{d}}{\mathrm{d}\chi}\left(v\mathcal{H}\frac{\mathrm{d}\mathcal{U}}{\mathrm{d}\chi}\right). \tag{5.4}$$
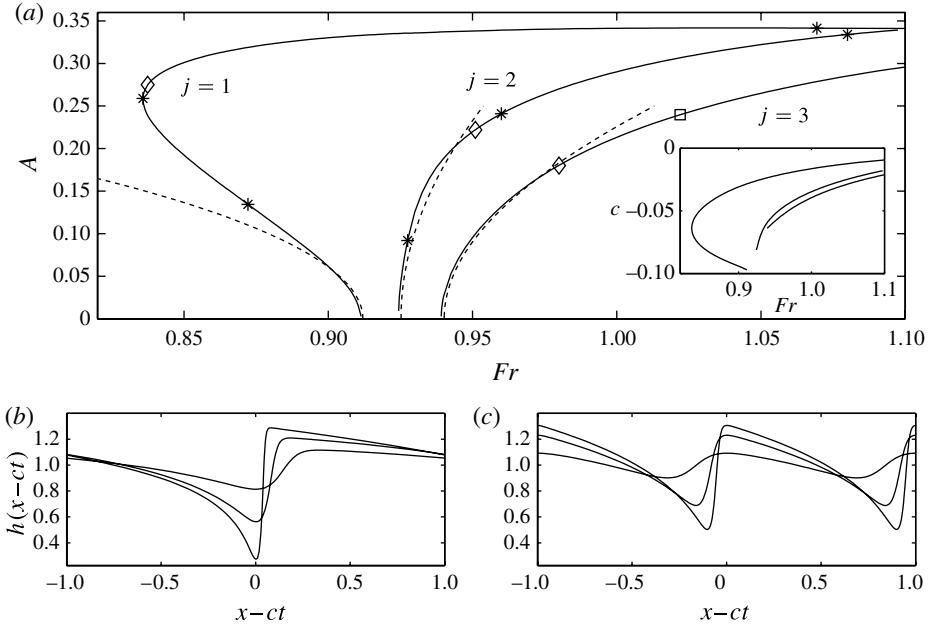
FIGURE 7. Bifurcation diagram and sample nonlinear waves for $L = 2$, $\nu = 0.02$ and $\varepsilon = 0.1$. Panel (*a*) shows the solution branches, $A = \sqrt{\langle (h-1)^2 \rangle}$ versus Fr, for the lowest three modes ($j = 1$, 2 and 3); the inset displays the corresponding wave speeds, c. The dashed lines show analytically constructed, weakly nonlinear solutions (see appendix B). To the right of the points marked by diamonds, the states suffer the short-wavelength secondary instability. To the right of the point marked by the square along the third branch, the coarsening instabilities disappear. Panels (*b,c*) show $h = \mathcal{H}(x - ct)$ for the $j = 1$ and 2 solutions at the Froude numbers marked by stars in (*a*) (wave amplitudes increase as one progresses along the solution branches).

After demanding that the solution be periodic, the eigenvalues, c and $\check{q}$, follow on breaking the translational invariance (by demanding, for example, that $\mathcal{H}(0) = 1$) and imposing the mass-conservation constraint, $\langle \mathcal{H} \rangle = 1$.

For $\varepsilon \ll 1$ and $c = O(\varepsilon)$, it is sufficient to take $q \approx \check{q}$ and $u \approx q/h$ in (5.3)–(5.4), in which case the system reduces to a form equivalent to the viscous generalization of the equations considered by Parker & Izumi. However, we do not include the extra condition that $u \to u_*$ at a point downstream of the smoothed hydraulic jump, which Parker & Izumi exploited to determine the wavelength of the cyclic steps. Instead, the wavelength here is determined simply by the length of our periodic domain, and the flow speeds take whatever values are required to satisfy (5.3)–(5.4).

By continuing the solutions to different Froude numbers and exploiting the amplitude measure A, we may construct bifurcation diagrams for the steady waves. Diagrams for the solutions corresponding to the end-states of figure 5 are shown in figure 7. The amplitudes of the two solutions with higher wavenumbers smoothly decline to zero at their respective critical Froude numbers, highlighting how they emerge supercritically at onset. The solution branch of the lowest mode, however, bifurcates subcritically (as found for antidunes by Colombini & Stocchino 2008) and only switches back to higher Froude numbers after a saddle-node bifurcation near $Fr \approx 0.836$. Given also that this mode is the first to become unstable, we conclude
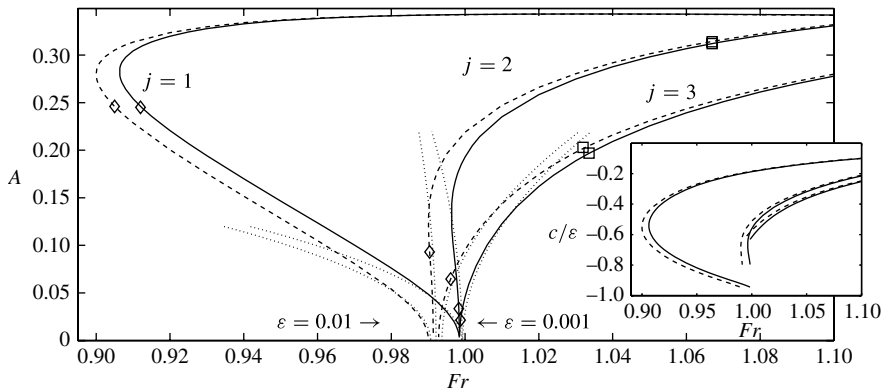
FIGURE 8. Bifurcation diagrams for $\varepsilon = 0.01$ (dashed lines) and 0.001 (solid lines), with $L = 2$ and $\nu = 0.02$. The main figure shows the solution branches for $j = 1$–3, and the inset displays the corresponding, scaled wave speeds, c/ε. The dotted lines show analytically constructed, weakly nonlinear solutions (see appendix B). Beyond the points marked by diamonds, the states suffer the short-wavelength secondary instability, and the coarsening instabilities disappear to the right of the squares marked on the $j = 2$ and 3 branches.

that the onset of cyclic steps is likely to be relatively abrupt, as noted earlier for the initial-value computations of figure 5.

The details of the bifurcation diagram in this window of parameter space is somewhat sensitive to the erosion parameter, ε: as illustrated in figure 8, there are quantitative, if not qualitative, changes to the structure when we reduce this parameter further and more closely approach the asymptotic, quasisteady limit. In particular, in that limit, the second ($j = 2$) branch also becomes subcritical and all the wave speeds c scale with ε (see figure 8). However, our overall conclusion regarding the relatively sudden onset of step patterns remains unchanged.

5.2. *Secondary instabilities*

Continuation of the computations of figure 5 to longer times reveals how the saturated states are not actually stable; see figure 9. As predicted by the asymptotic model of §4, the states with higher wavenumbers suffer a coarsening instability that prompts collisions of the component waves, leading to a single dominant structure in the domain. Unlike the predictions of that model, however, both the gravest state from figure 5 and the coarsened solutions display another, short-scale secondary instability. The secondary instabilities propagate at different wave speeds to the primary steps, leading to time-dependent patterns in all frames of reference.

Both the coarsening and short-wavelength instabilities can be confirmed by a direct linear stability analysis of the steady-wave states: we set

$$h = \mathcal{H}(\chi) + \hat{h}(\chi)e^{\lambda t}, \quad u = \mathcal{U}(\chi) + \hat{u}(\chi)e^{\lambda t}, \quad \zeta = \mathcal{Z}(\chi) - \varepsilon t \langle \mathcal{E}(\mathcal{U}) \rangle + \hat{\zeta}(\chi)e^{\lambda t},$$
(5.5)

where λ is the growth rate. Introducing this decomposition into the model equations and then linearizing in the perturbations amplitudes, $\hat{h}(\chi)$, $\hat{u}(\chi)$ and $\hat{\zeta}(\chi)$, leads to the normal-mode problem

$$\lambda \hat{h} - c \frac{d\hat{h}}{d\chi} + \frac{d}{d\chi}(\hat{h}\mathcal{U} + \mathcal{H}\hat{u}) = 0,$$
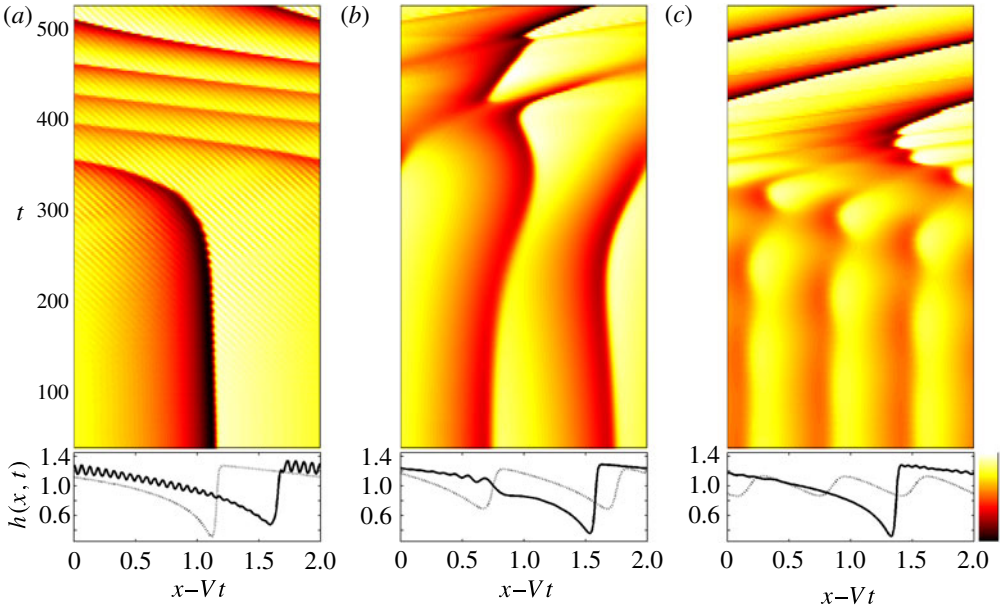(5.6)

FIGURE 9. (Colour online available at journals.cambridge.org/flm) Continuation of the initial-value problems in figure 5, showing $h(x, t)$ as a density on the $(x - Vt, t)$-plane, where $x - Vt$ refers to the frame travelling with the initial wavetrain (respectively, $V \approx -0.02$, -0.048 and -0.054). The initial and final snapshots of h are given immediately below each density plot, and indicate the shading scheme.

$$Fr^2 \left[\lambda \hat{u} - c \frac{\mathrm{d}\hat{u}}{\mathrm{d}\chi} + \frac{\mathrm{d}}{\mathrm{d}\chi} (\mathscr{U}\hat{u}) \right] = \frac{\mathscr{U}}{\mathscr{H}^2} (2\mathscr{H}\hat{u} - \mathscr{U}\hat{h}) - \frac{\mathrm{d}\hat{h}}{\mathrm{d}\chi} - \frac{\mathrm{d}\hat{\zeta}}{\mathrm{d}\chi}$$
$$+ \frac{1}{\mathscr{H}} \frac{\mathrm{d}}{\mathrm{d}\chi} \left(v \mathscr{H} \frac{\mathrm{d}\hat{u}}{\mathrm{d}\chi} \right) \qquad (5.7)$$

and

$$\lambda \hat{\zeta} - c \frac{\mathrm{d}\hat{\zeta}}{\mathrm{d}\chi} = -\varepsilon \mathscr{E}'(\mathscr{U})\hat{u}, \qquad (5.8)$$

which can be attacked numerically (cf. the comments in § 2.2).

The most unstable modes of the three states at $Fr = 0.96$ are shown in figure 10. The gravest solution has a short-wavelength instability that corresponds to the finely scaled features seen in figure 9(a). The most unstable modes of the $j = 2$ and 3 states, on the other hand, take the form of localized perturbations to the cyclic steps that translate those structures with respect to each other, prompting coarsening collisions. The $j = 2$ state also suffers a weaker short-wavelength instability (the two most unstable modes for $j = 3$ are both coarsening instabilities). Further computations demonstrate that both kinds of secondary instabilities (coarsening and short-wavelength) have growth rates, $\mathrm{Re}(\lambda)$, which scale with ε in the quasisteady limit.

By tracking the unstable modes along the solution branches, we find that the short-wavelength instabilities disappear at sufficiently low Froude numbers (marked by diamonds in figures 7 and 8). For the gravest solution at $\varepsilon = 0.1$, the short-wavelength secondary instability sets in very close to the saddle-node bifurcation that stabilizes
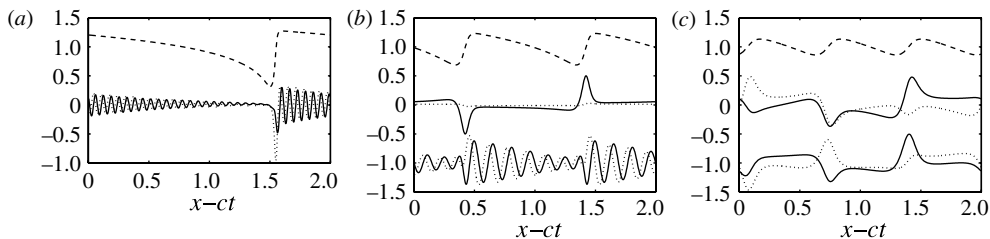
FIGURE 10. Unstable eigenfunctions for the three steady solutions at $Fr = 0.96$ in figures 5 and 6. The dashed lines show $\mathscr{H}(\chi)$; the solid and dotted lines show the real and imaginary parts of $\hat{h}(\chi)$. Panel (a) shows the most unstable mode for the $j = 1$ solution ($\lambda \approx 0.025 + 2i$). In (b) and (c), for the $j = 2$ and 3 solutions, the two most unstable modes are shown, with the weaker mode offset vertically by -1 ($\lambda \approx (9 + 8i) \times 10^{-3}$ and $0.006 + 2i$ in b and $\lambda \approx (1.3 + 5.7i) \times 10^{-2}$ and $(0.4 + 5.4i) \times 10^{-2}$ in c).

this branch beyond its subcritical birth. Thus, that solution exists as a stable steady state only over a very narrow range of Froude numbers. At lower erosion rates, we find that the gravest mode is never stable (figure 8). Hence, since the solution branches with $j > 1$ suffer both coarsening and short-wavelength instabilities, steady states are rare at best, and time-dependent cyclic-step patterns are more prevalent near onset. Despite this, the strength of the coarsening instabilities declines as one proceeds along the $j = 2$ and 3 solution branches and, for sufficiently high values of Fr, those modes actually become stable (see figures 7 and 8), indicating that coarsening no longer plays a key role in the dynamics at higher Froude numbers.

To understand the origin of the short-wavelength instability, we consider the limit, $\varepsilon \ll 1$ and $(c, \lambda) = O(\varepsilon)$, in (5.6)–(5.8). On discarding the terms with λ and c in (5.6)–(5.7) and retaining only the derivatives of the perturbation amplitudes in view of their short wavelength, we find

$$\mathscr{U}\hat{h} + \mathscr{H}\hat{u} \approx 0, \quad \nu \frac{\mathrm{d}^2\hat{u}}{\mathrm{d}\chi^2} - \frac{3\mathscr{U}}{\mathscr{H}}\hat{u} - \left(Fr^2\mathscr{U} - \frac{\mathscr{H}}{\mathscr{U}}\right)\frac{\mathrm{d}\hat{u}}{\mathrm{d}\chi} \approx \frac{\mathrm{d}\hat{\zeta}}{\mathrm{d}\chi}. \quad (5.9)$$

To deal with the erosion equation (5.8), we first note that the frequencies of the short-wavelength modes are relatively large (for the $j = 1$ solutions displayed in figures 7 and 8, the scaled frequencies at $Fr = 0.96$ are $\mathrm{Im}(\lambda)/\varepsilon \approx 20$, 24 and 25 for $\varepsilon = 0.1$, 0.01 and 0.001, respectively). Thus, the spatial derivative, $\mathrm{d}\hat{\zeta}/\mathrm{d}\chi$, is chiefly balanced by the frequency term, which implies a transformation back to the laboratory frame from the wave frame. In other words, the short-wavelength instability propagates much more slowly than the cyclic steps, a feature that is also very prominent in the nonlinear initial-value computations (the solution presented in figure 12 below provides the clearest illustration). Hence, we set

$$\lambda = ikc + \varepsilon\Lambda, \quad \hat{\zeta} = e^{ik\chi}B(\chi), \quad (5.10)$$

where $|kc| \gg |\Lambda|$, and the (more slowly varying) amplitude, $B(\chi)$, satisfies

$$\Lambda B - \frac{c}{\varepsilon}\frac{\mathrm{d}B}{\mathrm{d}\chi} \approx \frac{k\mathscr{E}'(\mathscr{U})B}{k(Fr^2\mathscr{U} - \mathscr{H}/\mathscr{U}) - i(\nu k^2 + 3\mathscr{U}/\mathscr{H})} \equiv \Delta(\chi)B, \quad (5.11)$$

given that $\mathrm{d}\hat{u}/\mathrm{d}\chi \to ik\hat{u}$ to leading order. If k is an integer multiple of $2\pi/L$, then $B(\chi)$ must be periodic and we may solve (5.11) and establish $\Lambda = \langle\Delta\rangle$. The growth
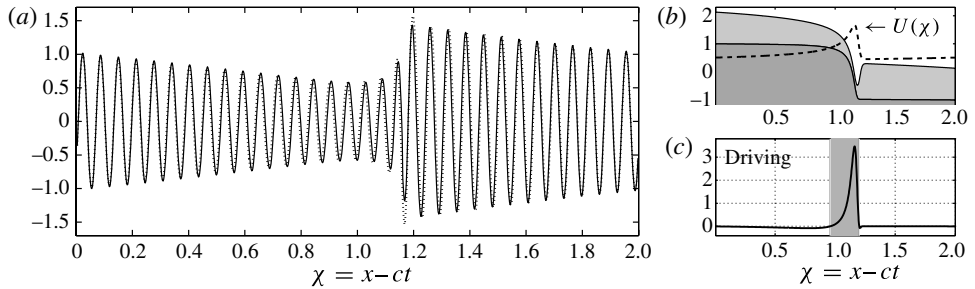
FIGURE 11. (*a*) A comparison of the real part of the most unstable eigenfunction, $\mathrm{Re}[\hat{\zeta}(\chi)]$ (dotted line), with the corresponding short-wavelength prediction (solid line) from (5.10)–(5.11), for the gravest cyclic-step solution (illustrated in *b*) with $Fr = 1.1$, $\nu = 0.02$, $L = 2$ and $\varepsilon = 0.001$. The eigenfunction and its approximation are normalized so that $\langle |\hat{\zeta}|^2 \rangle = 1$, and the phases are matched at $\chi = 0$. Panel (*c*) shows the 'driving density', $\mathrm{Re}(\Delta)$, from (5.11); the shaded region indicates where the local Froude number, $Fr \mathscr{U}/\sqrt{\mathscr{H}}$, exceeds unity.

rate is therefore

$$\mathrm{Re}(\varepsilon \Lambda) = \frac{1}{L} \int_0^L \frac{\alpha k^2 (Fr^2 \mathscr{U} - \mathscr{H}/\mathscr{U})\,\mathrm{d}\chi}{k^2 \left(Fr^2 \mathscr{U} - \mathscr{H}/\mathscr{U}\right)^2 + (\nu k^2 + 3\mathscr{H}/\mathscr{U})^2}, \qquad (5.12)$$

where $\alpha = \varepsilon \mathscr{E}'(\mathscr{U})$. The integrand of (5.12) is a *local* growth rate for perturbations with wavenumber, k, evolving about an equilibrium with $u = \mathscr{U}$ and $h = \mathscr{H}$. In fact, it is nothing more than the generalization of (3.4). In other words, the modal growth rate of the secondary instability is simply the spatial average of the growth rate for the erosional instability, computed using the nonlinear cyclic-step solution. Thus, the physical mechanism that drives the instability of the original cyclic step is also responsible for the secondary instability.

In figure 11, the short-wavelength prediction from (5.10)–(5.11) is compared to the numerically computed, most unstable eigenfunction, $\hat{\zeta}$, for the gravest cyclic step with $\varepsilon = 0.001$ and the other parameter settings quoted. For this particular mode, the eigenfunction exhibits 32 spatial oscillations over the domain and the frequency is positive. Hence, we take $k = -32\pi$, given that $L = 2$ and $c < 0$. We then use $\Lambda = \langle \Delta \rangle$ to estimate $\lambda/\varepsilon \approx 0.105 + 25.12\mathrm{i}$, which compares well with the computed value of $0.114 + 25.10\mathrm{i}$. The eigenfunction also compares surprisingly well with the approximation from (5.10)–(5.11), even though the modal wavelength is not that much smaller than the spatial scale characterizing the steepest part of the cyclic step.

Figure 11(*c*) plots the 'driving density', $\mathrm{Re}(\Delta)$, which determines the growth rate in (5.12). The cyclic-step bedform modifies the flow such that the local Froude number, $Fr \mathscr{U}/\sqrt{\mathscr{H}}$, falls below unity over most of the domain, reflecting how nonlinearity saturates the original step instability. However, the flow remains supercritical near the sharp face of the step, which is also where the erosion rates, and $\alpha = \varepsilon \mathscr{E}'$, are highest. Short-wavelength modes are able to take advantage of this localized driving region to precipitate secondary instability.

Note that the preceding arguments can be extended to indicate that the strongest secondary instabilities arise at the shortest wavenumbers as $\nu \to 0$, a feature that we also observed in suites of initial-value computations with varying ν. The mathematical difficulties encountered in the inviscid limit of the linear problem near onset are
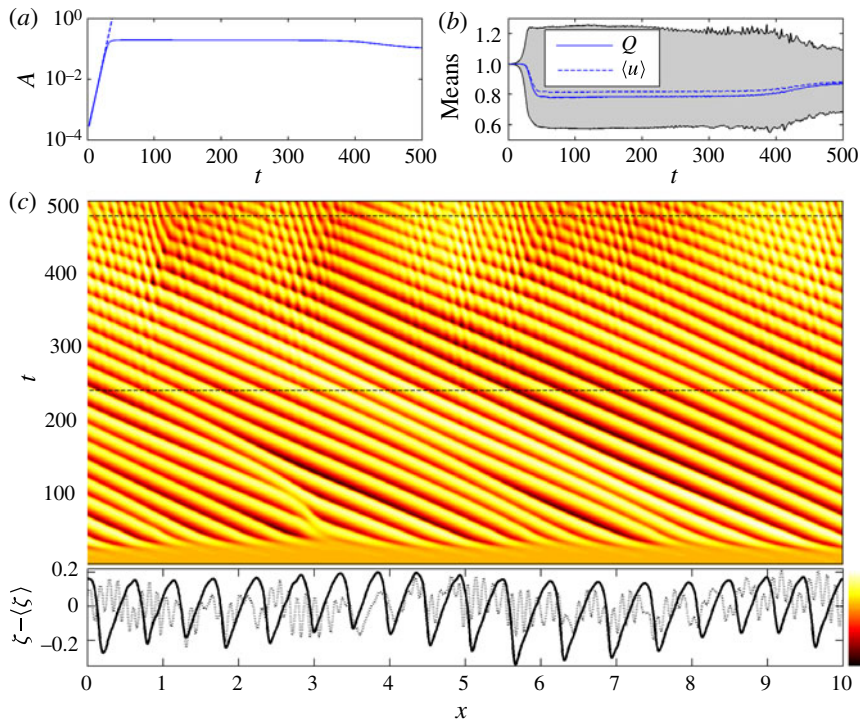
FIGURE 12. (Colour online) Cyclic steps at $Fr = 1.1$, $\nu = 0.02$, $L = 10$ and $\varepsilon = 0.1$. Panels (*a,b*) plot the amplitude, A, and means, $Q = \langle q \rangle$ and $\langle u \rangle$, against time; the shading in the second graph indicates the range of flow speeds within the domain. Panel (*c*) shows $\zeta - \langle \zeta \rangle$ as a density in the (x, t)-plane; the horizontal dashed lines indicate the times of the snapshots shown immediately below (with the later-time solution plotted as a dashed line), and indicate the shading scheme.

therefore also likely to carry over to the nonlinear dynamics, and viscosity is again an essential regularization.

5.3. *Further from onset*

To explore the dynamics further from onset, we consider a selection of Froude numbers and a wider domain ($L = 10$), beginning the initial-value problems from a uniform flow with additional, low-amplitude, random perturbations (see § 2.2). A solution at $Fr = 1.1$ is shown in figure 12 (part of this solution is also illustrated in figure 6). The instability is dominated by the most unstable linear modes, which have about 18 wavelengths in the domain in this example, and saturates without breaching the erosion threshold. Beyond saturation, there are a small number of coarsening events, but the pattern largely maintains its scale until it eventually degrades due to a short-scale, slower moving, secondary instability. Thus, the dynamics mirrors that found at smaller Froude numbers, except that the wavelength of the cyclic steps that appear initially is dictated largely by the fastest linear instability rather than the domain length (and, again, not by the erosion threshold). Over longer times, the cyclic-step patterns remain time-dependent, creating spatiotemporally complicated states characterized by a blend of the primary and secondary wavenumbers.

On raising the Froude number to 1.5 (figure 13), the character of the cyclic-step dynamics changes: the emergent patterns become sufficiently strong that they
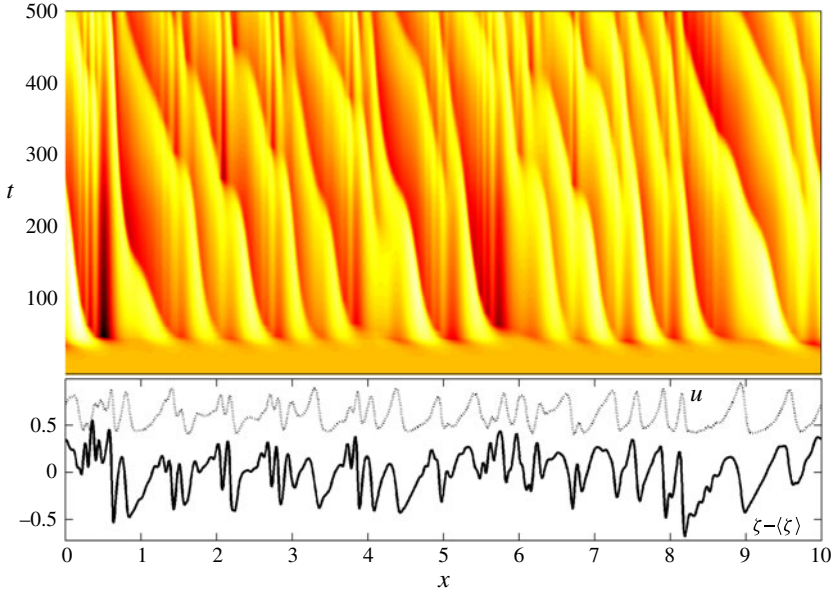
FIGURE 13. (Colour online) Cyclic steps at $Fr = 1.5$, $\nu = 0.05$, $L = 10$ and $\varepsilon = 0.1$. Panel (*a*) shows $\zeta - \langle \zeta \rangle$ as a density in the (x, t)-plane; the final snapshot is shown in (*b*). Also plotted (dashed) is the final snapshot of u.

appreciably block the water flux. (In periodic geometry, the St Venant equations conserve total mass, $\int_0^L h \, dx$, but not total flux, $\int_0^L hu \, dx$.) The stress on the bed is then reduced to the point that erosion is arrested over sections of the domain. A collage of migrating steps and static bedforms thereby develops with a complicated spatiotemporal pattern. The migrating steps gradually erode into the stationary bedforms to destroy those features, but the steps also deposit other, short-scale, bedforms in their wakes *via* the remnant of the secondary instability found at smaller Froude number.

By $Fr = 2$, the growth of the step instability blocks the flow so much that erosion is almost completely arrested (see figure 14). This leaves nearly stationary bedforms whose pattern reflects the structure of the linear instability and its modulation by the initial conditions. Over the sharper downward slopes, however, the flow speed can remain above threshold and some of the bedforms suffer further incision, steepening them into steps that slowly migrate upstream. However, the overall pattern bears little resemblance to a periodic cyclic-step sequence.

The preceding computations show no evidence of roll waves. As we raise the Froude number, the growth rate of these waves eventually exceeds that of the cyclic steps (whose time scale is controlled by ε), allowing roll waves to outgrow the cyclic steps from an arbitrary initial condition. This situation is the setting of the computation shown in figure 15. Initially, a roll wave grows out of the random initial perturbations and saturates into a steady nonlinear wave. However, bed erosion continues regardless of the relatively fast-moving disturbance in the overlying flow, and cyclic steps grow over a much longer time scale. The steps eventually reach sufficient amplitude to block the flow and destroy the roll wave. The reduction in flux switches off erosion altogether, leaving behind a stationary bedform. Note that the erosional instability is
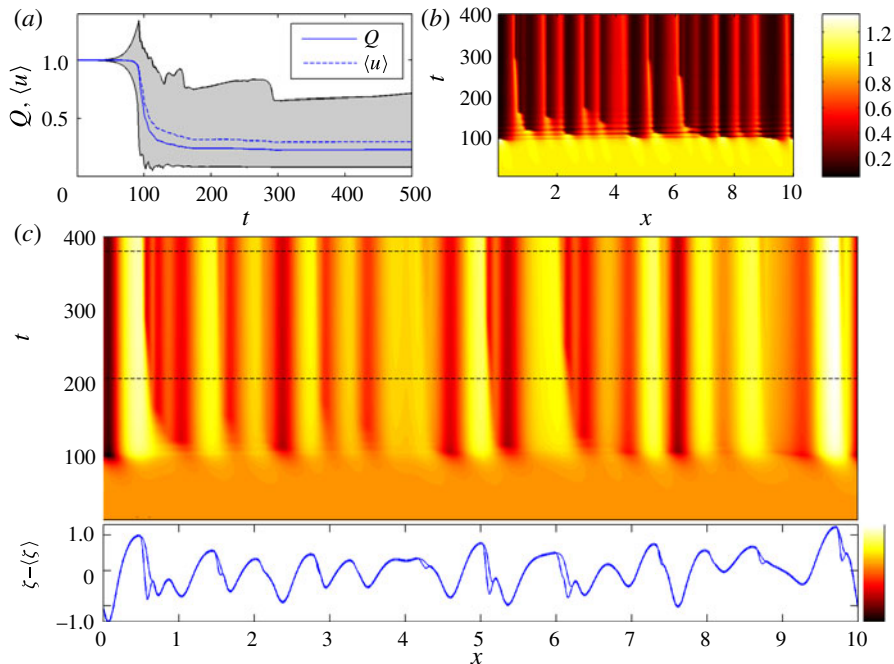
FIGURE 14. (Colour online) Cyclic steps at $Fr = 2$, $\nu = 0.1$, $L = 10$ and $\varepsilon = 0.1$. Panel (a) plots the means, $Q = \langle q \rangle$ and $\langle u \rangle$, against time; the shading indicates the range of flow speeds. Panels (b,c) show $u(x, t)$ and $\zeta - \langle \zeta \rangle$ as densities on the (x, t)-plane, respectively; the horizontal dashed lines in (c) indicate the times of the two snapshots shown immediately below.

relatively violent at this Froude number, generating a bedform pattern taking the form of a sequence of pools connected by shallow chutes.

5.4. *Non-periodic staircases*

A key feature of the dynamics uncovered above surrounds how cyclic steps block the water flux, thereby arresting erosion and stabilizing roll waves. Unfortunately, computations with periodic boundary conditions allow the reduction in water flow to recycle through the domain and permanently diminish the mean flux thereafter. To avoid such a global suppression of the flow, fluid must be allowed to enter the domain with a fixed flux through the upstream boundary. To explore this more physical scenario, we therefore abandon periodic boundary conditions and study the formation of non-periodic staircases.

To this end, we consider a domain of length $L = 100$ with fixed inflow conditions: $u(0, t) = h(0, t) = 1$. We allow fluid to leave the domain whilst generating as little disturbance as possible by adopting 'natural' outflow conditions: $h_x(L, t) = u_x(L, t) = 0$. Moreover, to further reduce any effect of the downstream boundary, we introduce an adjacent 'sponge layer' over which we increase the dissipation by replacing the constant eddy viscosity with $\nu(1 + e^{x-90})$. This sponge layer effectively removes any cyclic-step instability triggered by the exit conditions. Instead, to initiate the staircase, we begin initial-value computations with a uniform water flow ($h(x, 0) = u(x, 0) = 1$) over a more centrally perturbed bed: $\zeta(x, 0) = \zeta_0(x) \exp(-(x - 50)^2)$, where $\zeta_0(x)$ is a random superposition of the first 12 wavenumbers. We also terminate the computations
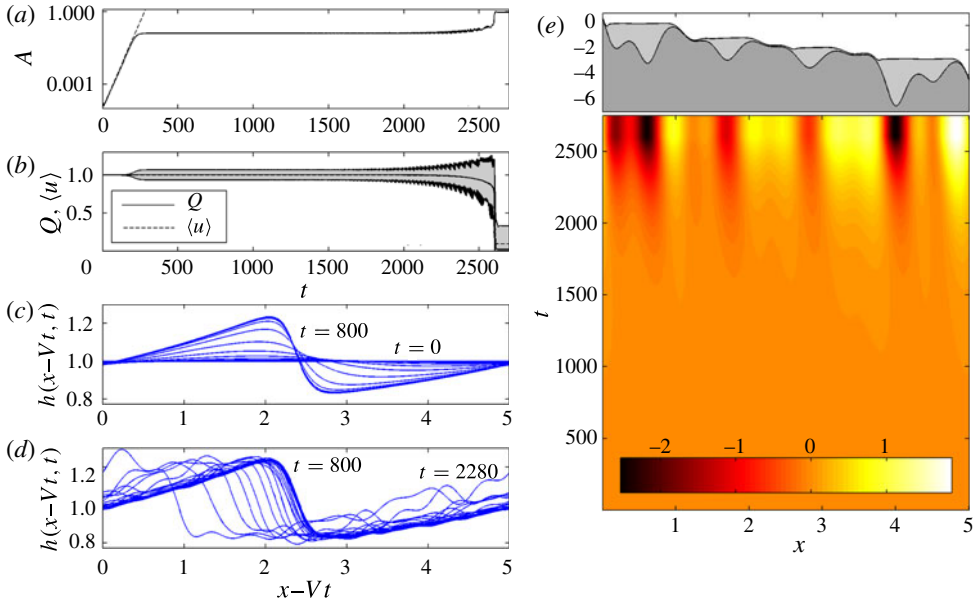
FIGURE 15. (Colour online) Roll waves and cyclic steps at $Fr = 3$, $\nu = 0.2$, $L = 5$ and $\varepsilon = 0.01$. Panels (*a,b*) plot the amplitude, A, and means, $Q = \langle q \rangle$ and $\langle u \rangle$; the shaded region in (*b*) shows the range of flow speeds. Panels (*c,d*) show snapshots of $h(x - Vt, t)$ in the frame of the roll wave (snapshots are spaced by 20 in *c* and 40 in *d*), for the times, $0 \leqslant t \leqslant 800$ and $800 \leqslant t \leqslant 2280$, respectively. Panel (*e*) shows $\zeta - \langle \zeta \rangle$ as a density on the (x, t)-plane, with the final bed structure and flow depth shown immediately on top.

once the steps reach the inflow; continuing beyond this moment is problematic for two reasons. First, the disappearance of the steps at the inflow triggers flow variations that rapidly sweep downstream to affect the entire staircase. Second, our numerical scheme experienced difficulty in accurately and stably capturing the collision of large steps with the boundary.

Figure 16 displays an initial-value computation with $Fr = 1.1$. In this instance, the localized initial perturbation in the bed generates a slowly varying train of cyclic-step waves that migrate largely upstream, but also develop downstream. The steps spread out and grow in amplitude as they propagate, with the strongest steps appearing near the front of the train. These bedforms once again cut down the flux and trap water, creating a distinctive 'shadow' in $q = hu$ downstream. This weakens the growth of the trailing steps, which, as a result, remain shallower, and a distinctive jump in the physical variables develops across the staircase. Only the stronger steps in the vanguard of the train amplify sufficiently to arrest erosion and, just before $t = 400$, the leading steps also suffer a short-wavelength secondary instability. Many of these features are in broad agreement with the periodic dynamics.

Qualitative changes are observed in the dynamics as one continues on to higher Froude numbers, some of which again echo our findings in periodic geometry. First, the steps now emerge relatively suddenly, generating significant interruptions in the water flux and prompting the formation of an upstream-propagating bore; see figure 17. The bore provides the primary blockage to the flow, severely reducing erosion in its wake for $Fr = 1.5$ and switching it off entirely for $Fr = 2$. This creates the wedge-like structure in the snapshots of $\zeta - x$ in the figures, with the staircase
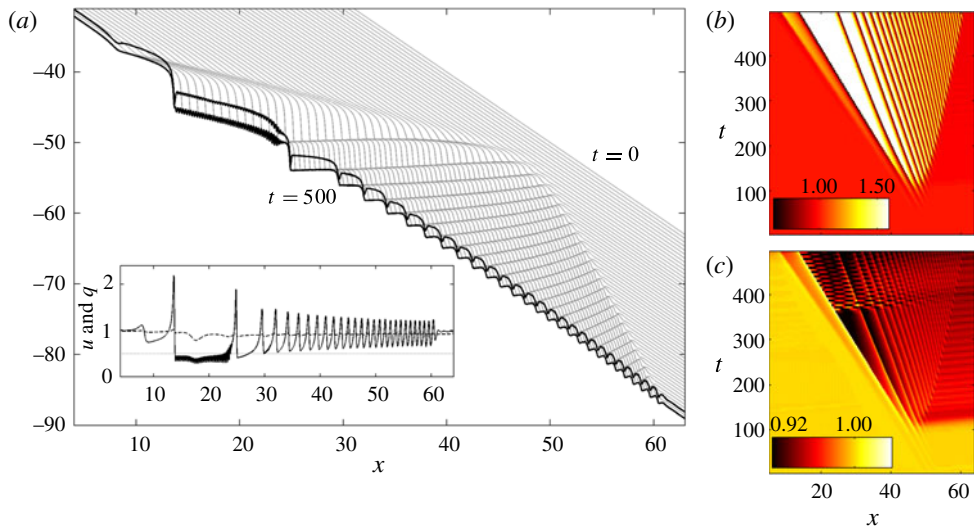
FIGURE 16. (Colour online) Staircases for $Fr = 1.1$, $\nu = 0.1$ and $\varepsilon = 0.1$ in a non-periodic domain of length $L = 100$. Panel (*a*) shows snapshots of $\zeta - x$ every 10 time units (lighter grey); the darker solid lines indicate the final bed profile and the water surface ($\zeta - x$ and $\zeta + h - x$ at $t = 500$). The inset shows $u(x, 500)$ (solid) and $q(x, 500)$ (dashed), along with the erosion threshold (dotted; $u_* = 0.5$). Panels (*b,c*) show h and q as densities in the (x, t)-plane: (*a*) $\zeta(x, t) - x$ and $\zeta(x, t) + h(x, t) - x$; (*b*) $h(x, t)$; (*c*) $q(x, t)$.

emerging only much further downstream. For $Fr = 1.5$, a mix of migrating and static bedforms characterizes the complex structure of the staircase. At $Fr = 2$, the cyclic-step instability generates large-amplitude, stationary undulations; erosion only takes place on their downstream faces, cutting into those features and forcing them to retreat upstream. In both cases, fresh bedforms gradually appear at the downstream edge of the staircase, each signalling its arrival with an interruption in water flux.

For all the solutions, the staircases spread out from the initial perturbation both upstream and downstream. Thus, as anticipated in § 3.3, the cyclic-step instability is evidently an absolute one. Indeed, if the computations are run long enough, roundoff errors excite the instability throughout the domain (except for the sponge layer), and steps appear abruptly everywhere.

6. Discussion

In this article we have explored the nonlinear dynamics of cyclic steps in a simple model of shallow-water flow over eroding topography (the St Venant equations coupled with an empirical Exner equation for sediment transport). These bedforms arise from a linear instability generated by the interaction between the flow dynamics and the erodible bed, and are expected once the flow becomes supercritical (Parker & Izumi 2000). Using a combination of analytical and numerical methods, we studied the nonlinear saturation of this instability, in order to quantify the cyclic-step patterns that form and gauge how they interact with roll waves, a hydrodynamic instability expected under similar physical conditions.

Previous work on cyclic steps has largely concentrated on constructing steadily propagating step patterns with the form of periodic wavetrains. These patterns consist of regular sequences of relatively abrupt steps in the bed with coincident hydraulic
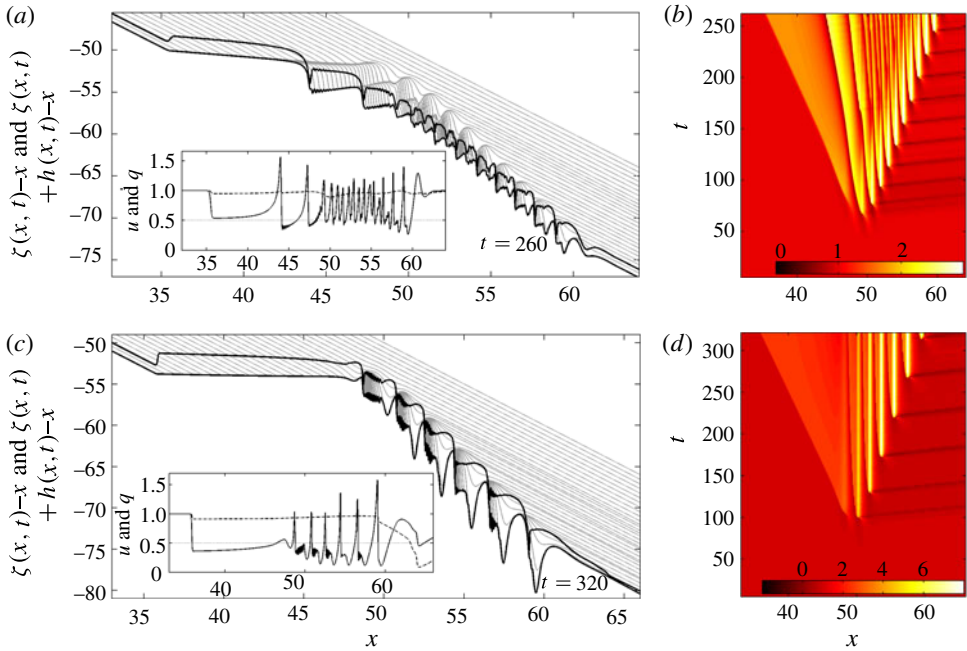
FIGURE 17. (Colour online) Non-periodic staircases for $Fr = 1.5$ (*a,b*) and $Fr = 2$ (*c,d*); $\nu = 0.1$ and $\varepsilon = 0.1$. Panels (*a,c*) show snapshots of $\zeta - x$ every 10 time units (lighter grey); the darker solid lines show $\zeta - x$ and $\zeta + h - x$ at the final times ($t = 260$ and 320, respectively). The insets show the final u (solid) and q (dashed), and the erosion threshold (dotted). Panels (*b,d*) show $h(x, t)$ as a density in the (x, t)-plane.

jumps in the overlying flow. Just beyond the onset of instability, we do observe patterns of this kind once the primary cyclic-step instability saturates. However, these states do not remain steady, but suffer short-wavelength secondary instabilities driven by the same mechanism that creates the steps themselves. As a result, complicated spatiotemporal patterns form that do not resemble regular step sequences, except, perhaps, very close to the critical Froude number. Further from onset, the formation of bedforms can reduce the water flux sufficiently to arrest erosion, leading to fixed patterns imprinted in the bed that coexist with migrating steps. The blocking of the flux also suppresses roll waves.

A key feature of our model for sediment transport is that it accounts only for erosion, not deposition. We have, however, made a brief exploration of an extension of the model that incorporates deposition (Sun & Parker 2005); details are given in appendix A. The main conclusion is that deposition does not change the dynamics outlined above in any significant way. On the other hand, the linear cyclic-step instability of Parker & Izumi (2000) is reliant upon the form of the erosion law; the transport law used by Colombini & Stocchino (2005), for example, furnishes no such instability, and generates the classical antidunes instead. We have sedulously avoided much discussion of this unfortunate consequence of empirical parameterization, and our main focus has been to explore the dynamics contained in the Parker & Izumi model without questioning its physical foundation. Our model also contains parameterizations of turbulent stresses; we have, at least, been able to demonstrate that the dynamics is insensitive to the form of the eddy viscosity used to regularize

hydraulic jumps and short-wave instabilities (we adopted a constant eddy viscosity, but the alternative choice in which this viscosity is proportional to water flux does not lead to significantly different results).

We close by contrasting the results with the experiments reported by Taki & Parker (2005). They observed recurrent isolated steps migrating slowly up a flume and saw no roll waves, despite favourable physical conditions. The lack of roll waves may well be due to their convective nature, implying that a constant agitation at the inlet is required to excite them. The recurrent steps, on the other hand, can be explained naturally in terms of the absolute cyclic-step instability. The experiments also show little sign of fine-scale secondary features superposed on the primary steps, suggesting that there are no short-wavelength secondary instabilities. We have no clear explanation for why such features are so prevalent in the model but not in the experiments; in all likelihood, they reflect inadequacies in the shallow-water approximation and the erosion law, and expose key limitations of the model.

Acknowledgements

Appendix A. Deposition

We include the effects of deposition by adding a new variable representing the depth-averaged concentration of the suspended load, $s(x, t)$, and then including a sedimentation term in the Exner equation (2.3):

$$\zeta_t = -\varepsilon \mathscr{E}(u) + ws, \tag{A 1}$$

where w is the sedimentation speed. The concentration satisfies the transport law

$$h(s_t + us_x) = \varepsilon \mathscr{E}(u) - ws + (\kappa h s_x)_x, \tag{A 2}$$

where κ is a turbulent diffusivity, which in practice we take to be the same as the eddy viscosity, $\kappa = \nu$ (i.e. the turbulent Schmidt number is unity). As discussed in §2, an alternative choice for κ might make this coefficient depend on water flux (specifically, $\kappa = \Lambda Fr^4 h|u|/c_f$); however, we have not explored such modifications in any detail.

Now the system of governing equations admits a uniform equilibrium solution in which erosion balances deposition:

$$h = u = 1, \quad \zeta = 0, \quad s = \frac{\varepsilon \mathscr{E}(1)}{w}. \tag{A 3}$$

A linear stability analysis of this state furnishes the dispersion relation

$$0 = Fr^2\lambda^3 + \lambda^2(2 + \nu k^2 + 2ikFr^2) + \lambda[k^2(1 - Fr^2) + ik(3 + \nu k^2 - \alpha)]$$
$$+ \alpha k^2 - \frac{i\alpha wk(\lambda + ik)}{\lambda + ik + w + \kappa k^2}, \tag{A 4}$$

which differs from (3.2) only by the last term. For $\alpha \ll 1$ and $\lambda = O(\alpha)$, (A 4) simplifies to

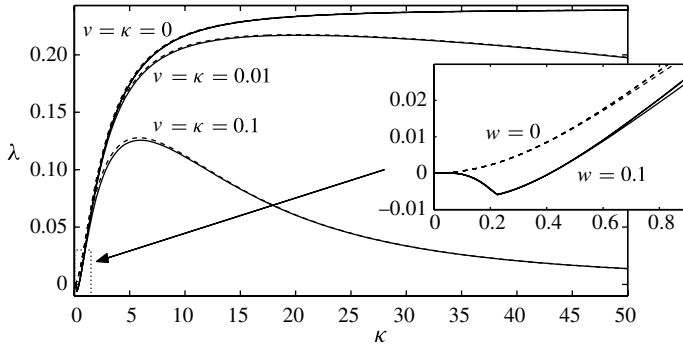$$\lambda \approx \frac{\alpha k^2(i\kappa k - 1)}{(ik + w + \kappa k^2)[3 + \nu k^2 + ik(1 - Fr^2)]}. \tag{A 5}$$

FIGURE 18. Growth rates of the most unstable modes against k for $Fr = 1.5$, $\nu = \kappa$, $\varepsilon = w = 0.1$ and the three values of ν indicated. The dashed lines show the corresponding results with $w = 0$, which are most easily distinguished in the magnified region at small k.

If we also take $(\nu, \kappa)k^2 \to 0$, we find the growth rate

$$\text{Re}(\lambda) \sim \frac{\alpha k^2 [k^2 (Fr^2 - 1) - 3w]}{(w^2 + k^2)[9 + k^2 (Fr^2 - 1)^2]}. \tag{A 6}$$

Thus, deposition stabilizes the long-wavelength modes, as further illustrated in figure 18. Note that the main differences with the purely erosive case arise at wavelengths that are longer than the computational domains considered in the main text. Thus, deposition does not modify the corresponding linear dynamics.

To discover the effect of deposition on the nonlinear dynamics close to the onset of instability, we repeat the asymptotics of §4, including the distinguished parameter selections, $\kappa = \delta\kappa_1$ and $w = \delta w_1$, and sequences

$$\zeta = \delta\zeta_1(x, t, T) + \delta^2\zeta_2(x, t, T) + \cdots, \quad s = \frac{\varepsilon\mathscr{E}(1)}{w} + \delta s_1(x, t, T) + \delta^2 s_2(x, t, T) + \cdots. \tag{A 7}$$

The result of the asymptotic machinations, including the rescalings in (4.12), is then the canonical amplitude equation

$$(1 - 2\partial_\xi)(\varphi_\tau + \varphi\varphi_\xi) + \varphi_\xi + \mu\varphi_{\xi\xi\xi} + \gamma\varphi\varphi_\xi + \Upsilon\varphi = 0, \tag{A 8}$$

where

$$\Upsilon = -\frac{2\alpha w_1}{f(1 - c)^2[1 + 2(1 - c)^2]}. \tag{A 9}$$

The effect of the final deposition term on the nonlinear dynamics described in §4.2 can be gauged by solving (A 8) numerically with $\Upsilon \neq 0$. A key result is that wave coarsening is arrested even if $\gamma = -1$. Thus, deposition also exerts a nonlinear control on wavelength selection.

To explore the effect of deposition on the dynamics further from onset, we numerically solved the full St Venant model in conjunction with (A 1) and (A 2), taking $w = \varepsilon = 0.1$ and $\nu = \kappa = 0.02$, and then varying Fr. The results were in both qualitative and quantitative agreement with those for pure erosion. Thus, we conclude that, for the range of parameters chosen, the dynamics described in the main text is largely unchanged by the inclusion of deposition.

Appendix B. Weakly nonlinear expansions

We construct steady, weakly nonlinear solutions to the asymptotic model (4.13) by introducing the asymptotic sequences $\mu = \mu_c + \epsilon^2 \mu_2$ and

$$\varphi = \epsilon A e^{i(kx + \epsilon^2 \omega \tau)} + \epsilon^2 B e^{2i(kx + \epsilon^2 \omega \tau)} + c.c. + \cdots, \tag{B 1}$$

where ϵ is a small parameter that we exploit to organize the asymptotics, μ_c denotes the critical value of μ, k is the basic wavenumber and ω is a frequency correction. We substitute these expressions into the governing equations and solve order by order. At order ϵ, we find the critical condition $\mu_c k^{-2} = 1$. At next order, the equations demand that

$$B = \tfrac{1}{6}(1 + 2\gamma - 4ik)A^2. \tag{B 2}$$

Finally, at $O(\epsilon^3)$, the terms involving $\exp i(kx - \omega t)$ provide an amplitude equation that predicts

$$|A|^2 = -\frac{3}{4}\mu_2 \left[1 + \frac{(1 + \gamma)(2 - \gamma)}{8k^2} \right]^{-1}. \tag{B 3}$$

Because the solution $\varphi = 0$ is linearly unstable for $\mu < \mu_c$ ($\mu_2 < 0$), and $\gamma \approx 0$ or -1 for our two instabilities, the weakly nonlinear branch is therefore supercritical.

A similar expansion can be performed for travelling-wave solutions to the full erosive St Venant model, which satisfy (5.3)–(5.4). We set

$$Fr^2 = Fr_c^2 + \epsilon^2 f_2, \tag{B 4}$$
$$c = c_0 + \epsilon^2 c_2, \tag{B 5}$$
$$q = (1 - c_0) + \epsilon^2 q_2, \tag{B 6}$$
$$\mathscr{H} = 1 + \epsilon a \sin k\chi + \epsilon^2 (a_2 \sin 2k\chi + a_3 \cos 2k\chi), \tag{B 7}$$
$$\mathscr{U} = 1 + \epsilon b \sin k\chi + \epsilon^2 (b_2 \sin 2k\chi + b_3 \cos 2k\chi + U_2) + \epsilon^3 b_4 \cos k\chi. \tag{B 8}$$

The amplitude parameter defined in (5.1) is related to a by $|A|^2 = \epsilon^2 |a|^2/2 + O(\epsilon^4)$. After eliminating $\mathscr{Z}$ and demanding that (5.3)–(5.4) are satisfied up to and including terms of order ϵ^3, we recover the critical conditions in (3.5) with $c = c_0$, and determine the coefficients, $\{c_2, q_2, a_2, a_3, b, b_2, b_3, U_2, b_4\}$, and the amplitude equation, $f_2 = \Gamma |a|^2$, where the coefficient, Γ, is a lengthy algebraic expression that we omit for sake of brevity. In this case, we find that the bifurcation can be subcritical, indicating that the weakly nonlinear limit does not commute with the asymptotic limit taken in § 4.

REFERENCES

BALMFORTH, N. J. 1995 Solitary waves and homoclinic orbits. *Ann. Rev. Fluid Mech.* **27**, 335–373.

BALMFORTH, N. J. & MANDRE, S. 2004 Dynamics of roll waves. *J. Fluid Mech.* **514**, 1–33.

BRIGGS, R. J. 1964 *Electron-Stream Interaction with Plasmas*. MIT.

COLOMBINI, M. & STOCCHINO, A. 2005 Coupling or decoupling bed and flow dynamics: fast and slow sediment waves at high Froude number. *Phys. Fluids* **17**, 036602.

COLOMBINI, M. & STOCCHINO, A. 2008 Finite-amplitude river dunes. *J. Fluid Mech.* **611**, 283–306.

CORNISH, V. 1910 *Ocean Waves and Kindred Geophysical Phenomena*. Cambridge University Press.

FAGHERAZZI, S. & SUN, T. 2003 Numerical simulations of transportional cyclic steps. *Comput. Geosci.* **29**, 1143–1154.

JEFFREYS, H. 1925 The flow of water in an inclined channel of rectangular bottom. *Phil. Mag.* **49**, 793.

KOSTIC, S., SEQUEIROS, O., SPINEWINE, B. & PARKER, G. 2010 Cyclic steps: a phenomenon of supercritical shallow flow from the high mountains to the bottom of the ocean. *J. Hydro-environ. Res.* **3**, 167–172.

KOYAMA, T. & IKEDA, H. 1998 Effect of riverbed gradient on bedrock channel configuration: a flume experiment. *Proc. Environ. Res. Centre Tsukuba Univ. Japan* **23**, 25–34.

KRANENBURG, C. 1992 On the evolution of roll waves. *J. Fluid Mech.* **245**, 249–261.

NEEDHAM, D. J. & MERKIN, J. H. 1984 On roll waves down an open inclined channel. *Proc. R. Soc. Lond.* A **394**, 259–278.

PARKER, G. 2008 Cyclic step formation: a phenomenon of supercritical shallow flow from the high mountains to the bottom of the ocean. In *Second Intl. Symp. Shallow Flow*. Hong Kong University of Science and Technology.

PARKER, G. & IZUMI, N. 2000 Purely erosional cyclic and solitary steps created by flow over a cohesive bed. *J. Fluid Mech.* **419**, 203–238.

PETZOLD, L. R. 1983 A description of DASSL – a differential algebraic solver. In *Scientific Computing* (ed. R. S. Stepleman), pp. 65–68. North-Holland.

SUN, T. & PARKER, G. 2005 Transportational cyclic steps created by flow over an erodible bed. Part 2. Theory and numerical simulation. *J. Hydraul. Res.* **43**, 502–514.

TAKI, K. & PARKER, G. 2005 Transportational cyclic steps created by flow over an erodible bed. Part 1. Experiments. *J. Hydraul. Res.* **43**, 488–501.

WINTERWERP, J. C., BAKKER, W. T., MASBERGEN, D. R. & VAN ROSSUM, H. 1992 Hyperconcentrated sand–water mixture flows over erodible bed. *J. Hydraul. Engng ASCE* **119**, 1508–1525.

YU, J. & KEVORKIAN, J. 1992 Nonlinear evolution of small disturbances into roll waves in an inclined open channel. *J. Fluid Mech.* **243**, 575–594.